### Observation of Ultraslow Shock Waves in a Tunable Magnetic Lattice

Jian Li<sup>®</sup>, S Chockalingam<sup>®</sup>, and Tal Cohen<sup>®</sup>1,3,\*

<sup>1</sup>Department of Civil and Environmental Engineering, Massachusetts Institute of Technology, Cambridge, Massachusetts 02139, USA

<sup>2</sup>Department of Aeronautics and Astronautics, Massachusetts Institute of Technology, Cambridge, Massachusetts 02139, USA

<sup>3</sup>Department of Mechanical Engineering, Massachusetts Institute of Technology, Cambridge, Massachusetts 02139, USA

(Received 29 January 2021; accepted 20 May 2021; published 29 June 2021)

The combination of fast propagation speeds and highly localized nature has hindered the direct observation of the evolution of shock waves at the molecular scale. To address this limitation, an experimental system is designed by tuning a one-dimensional magnetic lattice to evolve benign waveforms into shock waves at observable spatial and temporal scales, thus serving as a "magnifying glass" to illuminate shock processes. An accompanying analysis confirms that the formation of strong shocks is fully captured. The exhibited lack of a steady state induced by indefinite expansion of a disordered transition zone points to the absence of local thermodynamic equilibrium and resurfaces lingering questions on the validity of continuum assumptions in the presence of strong shocks.

DOI: 10.1103/PhysRevLett.127.014302

The propagation of shock waves in solids has received enormous attention in the last several decades [1–4]. Experiments, molecular dynamic simulations, and continuum mechanics modeling have been performed to investigate shock waves [5–8] and their interactions with complex material response such as plasticity [9], damage [10], dislocation and twinning [11–13], and phase transformation [14–16]. However, the microscopic mechanisms behind their formation are yet to be fully understood.

Since the first development of modern shock wave theory, it is widely accepted that, at the continuum scale, shock waves can be modeled as steadily propagating discontinuities within a medium [17]. While it is acknowledged that, in a physical system, even vanishing levels of viscosity or rate sensitivity promote a continuous waveform, the thickness of this wave is thought to be steady and infinitesimal compared to the scale of the continuum process [18]. Hence, the main features of shock wave propagation can be captured using one-dimensional rateindependent theories [19]. However, over the years, there have been indications of situations in which these assumptions break down [20–24]. Since the macroscopic response of a solid is intrinsically linked to its response at the microscopic scale, it is plausible that in these situations additional information on the microscopic process occurring within the narrow region of the shock is needed to explain the continuum level observations. However, to the best of our knowledge, the evolution and propagation of shock waves at the molecular scale has only been captured via numerical simulations [24-26]; whereas their direct observation can serve to better elucidate shock wave phenomena and to distinguish between artifacts of numerical modeling and the actual physics.

Packed granular chains serve as an example discrete system, which has been extensively studied due to its ability to generate strongly nonlinear waves, including shock waves [27] and Nesterenko solitary waves [28]. In these chains, the Hertzian contact between particles leads to their deformation in a highly nonlinear process, which is also responsible for significant energy dissipation. The response of these systems is thus not directly comparable to molecular-scale phenomena.

To mimic the molecular-scale response, we develop a desktop-scale experimental realization of shock wave evolution in a tunable magnetic lattice. We demonstrate the propagation of strong shocks and capture their entire evolution from a benign wave. Our validated numerical model provides a comprehensive understanding of the observed phenomena and its sensitivity to both external damping and the imposed waveform. Moreover, it confirms that this system supports the propagation of quasisteady strong shocks, in which the shock front exhibits "solitonlike" features propagating at constant velocity and strength, while the particle velocity profile reaches a steady oscillatory state. It is shown that for strong shocks a highly disordered transition regime emerges, from the shock front to the steady oscillatory state, and expands indefinitely, thus revealing an unsteady feature of shock waves that nucleates at the molecular scale and can grow to the macroscopic scale.

To realize shock wave evolution that is comparable to a molecular-scale process, but in a desktop-scale system, the experimental setup requires a tunable lattice with minimal levels of dissipation. Provided a finite imaging window, the system should evolve a benign impact into a shock within a prescribed propagation distance and at sufficiently slow velocities. The former can be achieved by particles with

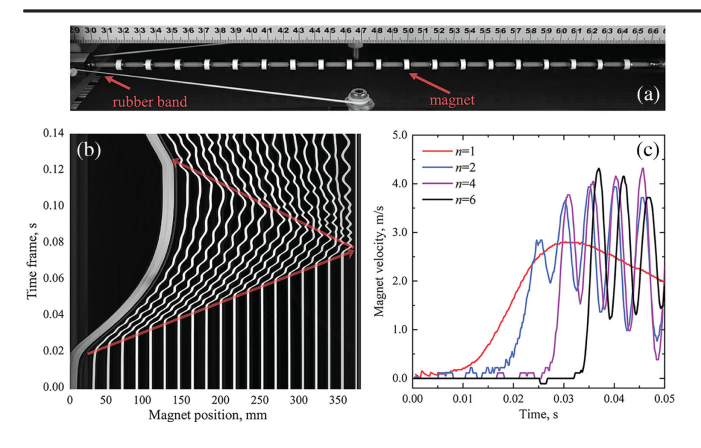


FIG. 1. Experimental setup and representative results with initial magnet separation  $r_0 = 12$  mm. (a) Experimental system consisting of magnet lattice threaded on a rigid rod. The impact pulse wave is generated by releasing the left magnet. (b) Magnet trajectories are shown as white curves, by vertically stacking images of the system at different times. (c) Magnet particle velocity profiles reconstructed via digital image correlation.

highly nonlinear repelling forces (i.e., strongly convex force-separation curve) and the latter by tuning the stiffness-to-mass ratio (i.e., the ratio between the local slope of the force-separation curve and the particle mass). To meet these requirements, we take advantage of the highly nonlinear repelling nature of rare-Earth magnets and construct a lattice of 21 particles with outer diameter of 6.35 mm, length of 6.35 mm, and mass of m = 1.084 g, as shown in Fig. 1(a). The magnets are free to slide on a nonmagnetic, minimal friction, supporting cylindrical rod. The first magnet (on the left) is attached to two tilted prestretched rubber bands through a plastic connector, while the last magnet is fixed. The magnets are initially equispaced and preloaded to tune the repulsive force (or, equivalently, the stiffness) before impact. The imparted wave is generated by releasing the first magnet, thus allowing the rubber bands to contract and initiate the propagation [see Fig. 1(b) and Video S1 [29]]. The dynamic process is recorded by a high-speed camera (Photron SA5,  $1280 \times 800$  pixels) at 8 kHz, allowing the measurement of magnet displacement, velocity, and acceleration via digital image correlation method. Using this setup the impact strengths and lattice stiffness are separately tuned by varying the prestretch of the rubber bands or the initial separation between the magnets, respectively. More details of the experimental system are given in Sec. S1 of the Supplemental Material [29].

To show that this system is capable of evolving an ordinary waveform into a shock, within the allocated propagation distance, we examine its response to an impact. The magnet trajectories are shown in Fig. 1(b) for the case with maximum impact velocity  $V_I = 2.81$  m/s and with an initial magnet separation of  $r_0 = 12$  mm. As indicated by the red arrow, the evolution of the magnet displacements

shows a wave propagating from the impacted end, into the lattice at  $V_P = 6.42$  m/s. Then, upon arrival at the last magnet, a reflection wave propagates back. It is seen from the displacement profiles that, although the imparted waveform is smooth, its propagation induces sharp oscillations in magnet particle displacement curves, indicating rapid changes in magnet velocities.

If a shock forms, the wave profile is expected to steepen. By examining the velocity profiles of different magnet particles in Fig. 1(c), it is clearly observed that in our system significant steepening occurs and is accompanied by oscillations that become more violent as propagation proceeds. In particular, notice the decreasing rise times (i.e., the duration from zero velocity to first peak velocity), which reduce from 23.9 ms for the first particle (n = 1) to 4.9 ms for n = 6. This result clearly demonstrates the realization of a longitudinal shock wave and its evolution from a simple wave. Moreover, the violent oscillations of increasing amplitude, in what seems to be a highly disordered process, are indicative of strong shocks.

To better understand the observed shock evolution, we numerically model the system as a chain of particles connected by nonlinear springs. In the following analysis, we only consider the interaction between first neighboring magnets. Although some influence may arise from the magnetic field of the non-nearest particles, it is a second-order effect (see Sec. S3 in the Supplemental Material [29]). Additionally, we neglect magnet rotations, and the length of the magnet is not considered in the calculation of propagation velocity. Accordingly, the equation of motion for the *n*th magnet reads

$$m\frac{d^2u_n}{dt^2} = F_{n-1} - F_n - f_n,\tag{1}$$

where  $u_n$  denotes the particle displacement, and  $F_n$  and  $f_n$ are the repulsive and frictional forces, respectively. In particular, based on experimental measurement of the force-displacement curve [Fig. 2(a)], the repulsive force is approximated using the formula  $F = K/(r+b)^q$ , where r is the separation between two neighbor particles, and the coefficient values are  $K = 413.8 \text{ N} \text{ mm}^3$ , b = 3.917 mm, and q = 3. A Coulomb model captures the influence of friction between the rod and the magnets via the formula  $f_n = \mu[mg + p(F_{n-1} + F_n)],$  where the coefficients  $\mu = 0.285$  and p = 0.012 are experimentally calibrated (see Supplemental Material Sec. S4 [29]), and g is the gravitational acceleration. The measured motion of the impacting magnet  $u_1(t)$  is given as a boundary condition at one end, while at the other end we impose  $u_{21}(t) = 0$ . The equations of motion are numerically solved using a finitedifference method [32]. Numerical results obtained using this model are compared with experimental curves for the second and eighth magnets in Figs. 2(b)-2(e) and show excellent agreement for the velocity profiles. The

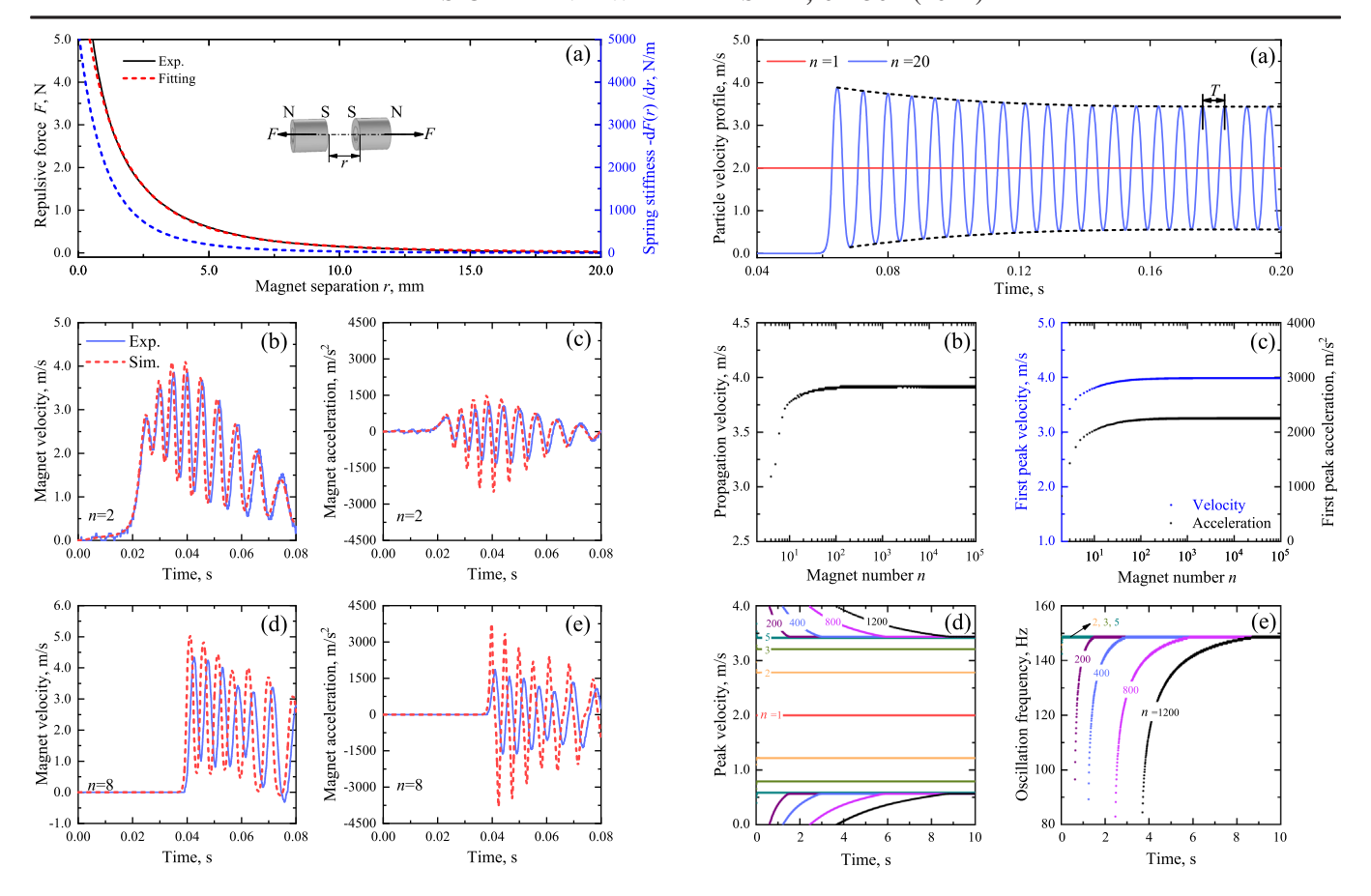


FIG. 2. Comparison of experimental and numerical results. (a) Force-displacement curve and instantaneous stiffness for the nearest magnet interaction. (b)–(e) Experimental (continuous blue lines) and numerical (dashed red lines) results for magnet particle velocities and accelerations. The uncertainties in the velocity and acceleration measurements are 0.16 m/s and  $170.67 \text{ m/s}^2$ , respectively. Details of the derivation process are shown in Sec. S2 of the Supplemental Material [29].

acceleration profiles are also well captured by the simulation. The discrepancy in peak accelerations can be explained by the limited image resolution (~20 pixels per ring magnet particle length), which is insufficient to capture sharp changes in acceleration (see Sec. S2 of the Supplemental Material [29]).

Next, we use our calibrated model to investigate the long-time behavior of strong shocks. For simplicity, we consider a long lattice subjected to a constant impactor velocity (a long lattice is used to avoid wave reflections). Figure 3(a) shows a typical velocity profile obtained for an impactor velocity of  $V_I = 2 \text{ m/s}$ , in the absence of friction. Upon arrival of the shock front, the particle velocity is shown to rapidly increase to 3.87 m/s, followed by strong oscillations with a decaying amplitude. Unlike a linear system, for which the vibration amplitude decays completely (see Supplemental Material Secs. S5 and S9 [29]), a stable finite-amplitude oscillation about the impactor velocity is eventually attained. Note that this motion is

FIG. 3. Long-time dynamic response of the system without friction. (a) Typical velocity profile of a particle. (b) Variation of propagation velocity as the wave progresses through particles into the lattice. (c) First peak velocity and first peak acceleration of each particle. (d) Evolution of peak velocity (both local maximum and minimum peaks) with time for various particles. (e) Evolution of oscillation frequency with time for various particles. Results are shown for the system with initial separation  $r_0 = 12$  mm.

nonharmonic due to the nonlinearity of the system. Examining the corresponding propagation velocity of the shock front in Fig. 3(b), we show that it gradually approaches a constant value of  $V_P = 3.92 \text{ m/s}$ . It is notable that this stabilized propagation velocity is significantly larger than the impactor velocity and the linear propagation velocity  $V_0 = 1.62 \text{ m/s}$  [33]. If frictional effects are included, a gradual decay of the propagation velocity is expected beyond a peak value (see Sec. S6 in the Supplemental Material [29]). Nonetheless, once developed, the early-time propagation velocity (i.e., for the first  $\sim$ 20 magnets) is comparable to the propagation velocity in the frictionless system. Figure 3(c) shows that both the first peak velocity and the first peak acceleration increase with increasing particle number, which is an intrinsic feature of strong shock waves. Eventually, the competition between nonlinearity and dispersion in the system results in

saturation of the first peak velocity and peak acceleration. In particular, the saturated first peak velocity is  $2V_I$ .

Further, to understand the transition from the wave front to the stabilized oscillatory state, Figs. 3(d) and 3(e) present the peak velocity and the corresponding oscillation frequency for different particle numbers as a function of time. We find that both the amplitude and the period decrease with time; moreover, after a rapid increase in stabilized oscillation amplitude (from the first magnet to the fifth magnet), the following particles arrive at the same oscillatory state (same amplitude and same period). Nonetheless, it is observed that the time of transitioning from peak velocity to the stabilized state is longer for the larger particle numbers, resulting in the highly disordered transition zone that expands indefinitely as the shock front penetrates deeper into the undisturbed lattice (see Video S2 [29]). Analogous to the interpretation of molecular-scale response, the finite-amplitude steady oscillation in the wake of a shock is consistent with an increase in temperature [34], whereas the disordered transition region appears to be out of thermodynamic equilibrium and its growth can be attributed to increasing entropy.

To further understand the range of shock wave response realized in our experiments, we explore the effect of the impactor velocity on the propagation velocity of the quasisteady shock wave in Fig. 4(a). The nearly linear dependence observed in both experimental and numerical results resembles the reported experimental findings of shock Hugoniot data in metallic materials [35] and molecular simulations of shock waves [36]. The agreement between theory and experiments is shown with slight deviations attributed primarily to effects of friction and the precise form of the imparted wave that is neglected in the simulation (see Supplemental Material Secs. S6 and S7 [29]). While these curves, as well as the corresponding oscillation frequency [Fig. 4(b)], do not reveal information on the shock strength, we examine in Fig. 4(c) the kinetic energy associated with the steady-state oscillation. Quite noticeably, the increase in oscillation energy becomes pronounced beyond a critical impactor velocity  $V^*$ , which is smaller than the linear propagation velocity (i.e.,  $V^* < V_0$ ). This threshold velocity represents the transition into the strong shock regime, which is characterized by a dramatic increase in energetic consumption.

In the absence of a unified quantitative definition of strong shocks, which are typically distinguished from weak and moderate shocks by virtue of the *very large* magnitude jump in field variables that they impose [37], here we propose a quantitative definition of strong shocks based on the oscillation energy ratio, which is directly linked to the level of energy dissipation. We identify the critical impact velocity  $V^*$  for the onset of a strong shock as velocity at which the curvature of the oscillation energy ratio curve changes sign, namely  $d^2\eta/dV_I^2=0$  [see inset in Fig. 4(d)]. Accordingly, strong shocks occur for  $V_I>V^*$ , and

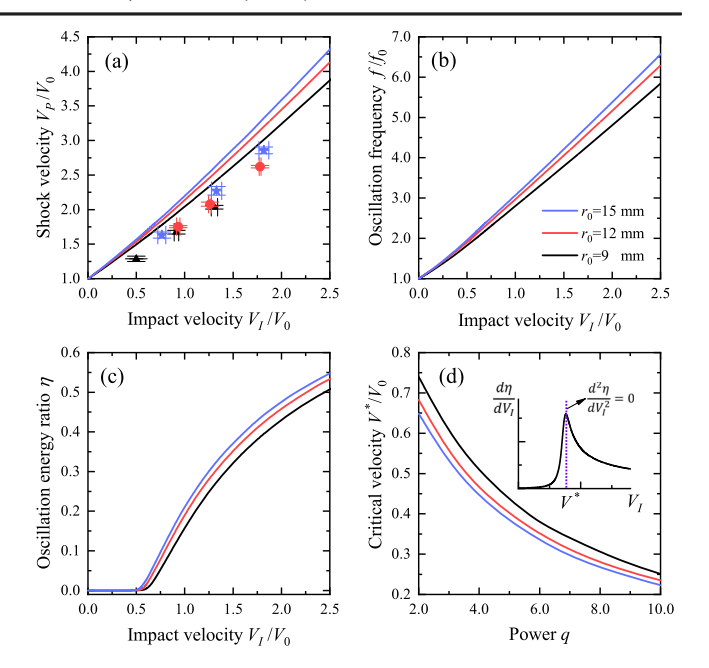


FIG. 4. Dependence of the stabilized shock response on impact velocity. Curves represent numerical solutions. Experimental data are shown as colored markers with error bars. (a) Shock wave propagation velocity. (b) Stabilized oscillation frequency f. (c) Oscillation energy ratio  $\eta$ . (d) Critical velocity. Here  $f_0$  represents the linear oscillation frequency, defined as  $f_0 = 1/\pi \sqrt{-(1/m)dF(r)/dr}|_{r=r_0}$ , and  $\eta = 1/T \int_{t_0}^{t_0+T} [V(t)/V_I - 1]^2 dt$ , where T = 1/f. If the oscillation is harmonic,  $\eta = 0.5$ .

moderate shocks occur in the finite range  $V_I \in (0, V^*)$ . A weak shock appears at the limit  $V_I \to 0$  [38]. From this definition it is clear that strong shocks are observed in our experiments [see Fig. 4(a)]. Moreover, despite the 8 orders of magnitude difference in length scale, the desktop-scale magnet lattice system preserves the key quantitative features of shock wave propagation in an analogous atomic system (as compared to a copper atomic lattice in Sec. S8 of the Supplemental Material [29]).

In Fig. 4(d), we further investigate this critical threshold by examining the influence of the stiffening law or, in particular, the power q. We observe that a system with increased stiffening can be driven beyond the critical threshold by lower impactor velocities.

In conclusion, we have shown that the desktop-scale experimental system presented here allows for complete spatiotemporal capture of the evolution of strong shocks from benign imparted waveforms. This is facilitated by taking advantage of the highly nonlinear repelling force between neighboring rare-earth magnets in a tunable one-dimensional lattice. Comprehensive investigation of the lattice response uncovers behaviors of strong shocks, which agree with predictions from molecular dynamic simulations. Hence, this Letter gives rise to a new avenue for

investigation of shock wave phenomena at the microscopic scale. Moreover, through this analysis, we observe the formation of a highly disordered transition region in the wake of strong shocks. This region nucleates at the particle scale, but continues to grow indefinitely. Observation of this phenomena at the macroscale, raises questions on the validity of continuum assumptions in the presence of strong shocks. Future work can take advantage of this system to expand beyond uniaxial propagation and can include additional physical effects, such as structure defects, thermal vibrations, and dissipation. Moreover, it is worth mentioning that the current design could also be modified to explore other nonlinear wave phenomena, such as solitons [39–41], elastic band gaps [42], and nonreciprocal waves [43–45].

The authors wish to acknowledge the financial support of the Army Research Office, under Grant No. W911NF-19-1-0275 and support from the National Science Foundation (CMMI, MOMS, 1942016).

- \*Corresponding author. talco@mit.edu
- [1] R. McQueen and S. Marsh, Equation of state for nineteen metallic elements from shock-wave measurements to two megabars, J. Appl. Phys. **31**, 1253 (1960).
- [2] B. L. Holian and P. S. Lomdahl, Plasticity induced by shock waves in nonequilibrium molecular-dynamics simulations, Science 280, 2085 (1998).
- [3] Y. Yao, Z. Huang, P. Xie, L. Wu, L. Ma, T. Li, Z. Pang, M. Jiao, Z. Liang, J. Gao *et al.*, High temperature shockwave stabilized single atoms, Nat. Nanotechnol. 14, 851 (2019).
- [4] S. A. Simmons, F. A. Bayocboc, Jr., J. C. Pillay, D. Colas, I. P. McCulloch, and K. V. Kheruntsyan, What is a Quantum Shock Wave? Phys. Rev. Lett. 125, 180401 (2020).
- [5] S. Catheline, J.-L. Gennisson, M. Tanter, and M. Fink, Observation of Shock Transverse Waves in Elastic Media, Phys. Rev. Lett. 91, 164301 (2003).
- [6] D. Espíndola, S. Lee, and G. Pinton, Shear Shock Waves Observed in the Brain, Phys. Rev. Applied 8, 044024 (2017).
- [7] S. Chockalingam and T. Cohen, Shear shock evolution in incompressible soft solids, J. Mech. Phys. Solids 134, 103746 (2020).
- [8] K. T. Ramesh, High rates and impact experiments, in *Springer Handbook of Experimental Solid Mechanics*, edited by W. N. Sharpe (Springer US, Boston, MA, 2008), pp. 929–960.
- [9] M. Chen, J. McCauley, D. Dandekar, and N. Bourne, Dynamic plasticity and failure of high-purity alumina under shock loading, Nat. Mater. 5, 614 (2006).
- [10] S. Fensin, J. Escobedo, G. Gray III, B. Patterson, C. Trujillo, and E. Cerreta, Dynamic damage nucleation and evolution in multiphase materials, J. Appl. Phys. 115, 203516 (2014).
- [11] A. Higginbotham, M. J. Suggit, E. M. Bringa, P. Erhart, J. A. Hawreliak, G. Mogni, N. Park, B. A. Remington, and J. S. Wark, Molecular dynamics simulations of

- shock-induced deformation twinning of a body-centered-cubic metal, Phys. Rev. B 88, 104105 (2013).
- [12] C. Wehrenberg, D. McGonegle, C. Bolme, A. Higginbotham, A. Lazicki, H. Lee, B. Nagler, H.-S. Park, B. Remington, R. Rudd *et al.*, In situ x-ray diffraction measurement of shock-wave-driven twinning and lattice dynamics, Nature **550**, 496 (2017).
- [13] S. J. Turneaure, P. Renganathan, J. M. Winey, and Y. M. Gupta, Twinning and Dislocation Evolution during Shock Compression and Release of Single Crystals: Real-Time X-Ray Diffraction, Phys. Rev. Lett. 120, 265503 (2018).
- [14] G. Duvall and R. Graham, Phase transitions under shockwave loading, Rev. Mod. Phys. **49**, 523 (1977).
- [15] K. Kadau, T. C. Germann, P. S. Lomdahl, and B. L. Holian, Microscopic view of structural phase transitions induced by shock waves, Science 296, 1681 (2002).
- [16] N. Amadou, T. de Resseguier, A. Dragon, and E. Brambrink, Coupling between plasticity and phase transition in shock-and ramp-compressed single-crystal iron, Phys. Rev. B 98, 024104 (2018).
- [17] M. D. Salas, The curious events leading to the theory of shock waves, Shock Waves 16, 477 (2007).
- [18] R. Courant and K. Friedrichs, Supersonic Flow and Shock Waves (Interscience, New York, 1948).
- [19] T. Von Karman and P. Duwez, The propagation of plastic deformation in solids, J. Appl. Phys. **21**, 987 (1950).
- [20] J. Hsu and R. Clifton, Plastic waves in a rate sensitive material—i. Waves of uniaxial stress, J. Mech. Phys. Solids 22, 233 (1974).
- [21] A. Molinari and G. Ravichandran, Fundamental structure of steady plastic shock waves in metals, J. Appl. Phys. **95**, 1718 (2004).
- [22] J. K. Knowles, Impact-induced tensile waves in a rubberlike material, SIAM J. Appl. Math. **62**, 1153 (2002).
- [23] J. Niemczura and K. Ravi-Chandar, On the response of rubbers at high strain rates—ii. Shock waves, J. Mech. Phys. Solids **59**, 442 (2011).
- [24] B. L. Holian and G. K. Straub, Molecular dynamics of shock waves in one-dimensional chains, Phys. Rev. B 18, 1593 (1978).
- [25] D. H. Tsai and C. Beckett, Shock wave propagation in cubic lattices, J. Geophys. Res. **71**, 2601 (1966).
- [26] B. L. Holian and G. K. Straub, Molecular Dynamics of Shock Waves in Three-Dimensional Solids: Transition from Nonsteady to Steady Waves in Perfect Crystals and Implications for the Rankine-Hugoniot Conditions, Phys. Rev. Lett. 43, 1598 (1979).
- [27] A. Molinari and C. Daraio, Stationary shocks in periodic highly nonlinear granular chains, Phys. Rev. E 80, 056602 (2009).
- [28] V. F. Nesterenko, Propagation of nonlinear compression pulses in granular media, J. Appl. Mech. Tech. Phys. **24**, 733 (1983).
- [29] See Supplemental Material at http://link.aps.org/supplemental/10.1103/PhysRevLett.127.014302 for more details on (S1) experimental details, (S2) estimation of uncertainty in velocity and acceleration derivation, (S3) measurement of the magnetic interaction force, (S4) calibration of the Coulomb friction coefficient, (S5) dynamic

- response of a linear lattice, (S6) effect of friction on propagation velocity, (S7) effect of loading profile in the nonlinear system, (S8) quantitative comparison of magnetic system and copper atom lattice, and (S9) effect of impactor velocity on the dynamic response of the nonlinear system, which includes Refs. [30,31].
- [30] C. Robbe, N. Nsiampa, A. Oukara, and A. Papy, Quantification of the uncertainties of high-speed camera measurements, Int. J. Metrol. Qual. Eng. 5, 201 (2014).
- [31] Ş. Erkoç, Empirical potential energy functions used in the simulations of materials properties, Annu. Rev. Comput. Phys. IX, 1 (2001).
- [32] R. J. LeVeque, Finite Difference Methods for Ordinary and Partial Differential Equations: Steady-State and Time-Dependent Problems (SIAM, Philadelphia, 2007).
- [33] Here, the linear velocity refers to the propagation velocity of small amplitude disturbances, which can be calculated as  $V_0 = r_0 \sqrt{-(1/m)dF(r)/dr|_{r=r_0}}$ , where  $r_0$  represents the initial magnet separation.
- [34] G. K. Straub, B. L. Holian, and R. G. Petschek, Molecular dynamics of shock waves in one-dimensional chains. ii. Thermalization, Phys. Rev. B **19**, 4049 (1979).
- [35] S. P. Marsh, LASL Shock Hugoniot Data (University of California Press, Berkeley, 1980), Vol. 5.
- [36] T. Hill and L. Knopoff, Propagation of shock waves in onedimensional crystal lattices, J. Geophys. Res. 85, 7025 (1980).

- [37] R. Courant and K. O. Friedrichs, Supersonic Flow and Shock Waves, Applied Mathematical Sciences Vol. 21 (Springer Science & Business Media, New York, 1999).
- [38] Weak shocks are simple waves up to second-order approximation in the shock strength [37].
- [39] B. Deng, J. R. Raney, V. Tournat, and K. Bertoldi, Elastic Vector Solitons in Soft Architected Materials, Phys. Rev. Lett. 118, 204102 (2017).
- [40] B. Deng, C. Mo, V. Tournat, K. Bertoldi, and J. R. Raney, Focusing and Mode Separation of Elastic Vector Solitons in a 2d Soft Mechanical Metamaterial, Phys. Rev. Lett. 123, 024101 (2019).
- [41] Y. Zhang, B. Li, Q. Zheng, G. M. Genin, and C. Chen, Programmable and robust static topological solitons in mechanical metamaterials, Nat. Commun. 10, 5605 (2019).
- [42] B. Deng, P. Wang, Q. He, V. Tournat, and K. Bertoldi, Metamaterials with amplitude gaps for elastic solitons, Nat. Commun. 9, 3410 (2018).
- [43] Y. Wang, B. Yousefzadeh, H. Chen, H. Nassar, G. Huang, and C. Daraio, Observation of Nonreciprocal Wave Propagation in a Dynamic Phononic Lattice, Phys. Rev. Lett. 121, 194301 (2018).
- [44] H. Nassar, B. Yousefzadeh, R. Fleury, M. Ruzzene, A. Alù, C. Daraio, A. N. Norris, G. Huang, and M. R. Haberman, Nonreciprocity in acoustic and elastic materials, Nat. Rev. Mater. 5, 667 (2020).
- [45] M. Brandenbourger, X. Locsin, E. Lerner, and C. Coulais, Non-reciprocal robotic metamaterials, Nat. Commun. 10, 4608 (2019).

# Observation of Ultraslow Shock Waves in a Tunable Magnetic Lattice Supplementary Material

Jian Li, S Chockalingam, and Tal Cohen, a, \*

<sup>1</sup>Department of Civil and Environmental Engineering, Massachusetts Institute of Technology, Cambridge, MA, 02139, USA

<sup>2</sup>Department of Aeronautics and Astronautics, Massachusetts Institute of Technology, Cambridge, MA 02139, USA

<sup>3</sup>Department of Mechanical Engineering, Massachusetts Institute of Technology, Cambridge, MA, 02139, USA

\*Corresponding author: talco@mit.edu

#### S1. EXPERIMENTAL DETAILS

The experimental setup is shown in Fig. S1. The system consists of a lattice of ring magnet particles, which is threaded along the rod such that the polarity of neighboring magnets has an opposite orientation (i.e. [N-S]-[S-N]-...-[N-S]-[S-N]), thus exerting a repulsive force. Each magnet particle is composed of two ring magnets with outer diameter of 6.35 mm, inner diameter of 3.175 mm, length of 3.175 mm, and mass of 0.542 g (KJ Magnetics Inc, Grade N42, R422). The rod has an outer diameter of 3.150 mm and is made of epoxy resin with fiberglass fabric reinforcement (McMaster-Carr, High-Temperature Garolite G-11 Rod). The rod with fixed ends on an aluminum alloy rail, is pre-stretched to minimize bending deformations. Both magnets and rod were lubricated by a PTFE based lubricant to reduce the friction. The last magnet on the left side is fully fixed to the rod. The first magnet on the right side is attached to two tilted pre-stretched rubber bands through a plastic connector. The magnets are disturbed to be equispaced. Note that we wait long enough to ensure that all magnets are in static equilibrium before initiating the propagation. In addition, each magnet is covered by a white label, to enhance contrast for optical tracking. Finally, a pulse wave is generated by releasing the first magnet, which then propagates into the lattice. The dynamic process is recorded using a high-speed camera (Photron SA5, 1280 x 800 pixels) at 8 kHz. The space resolution of recorded images is 0.30 mm. The magnet displacement is obtained via a specialized Matlab Digital Image Correction (DIC) code.

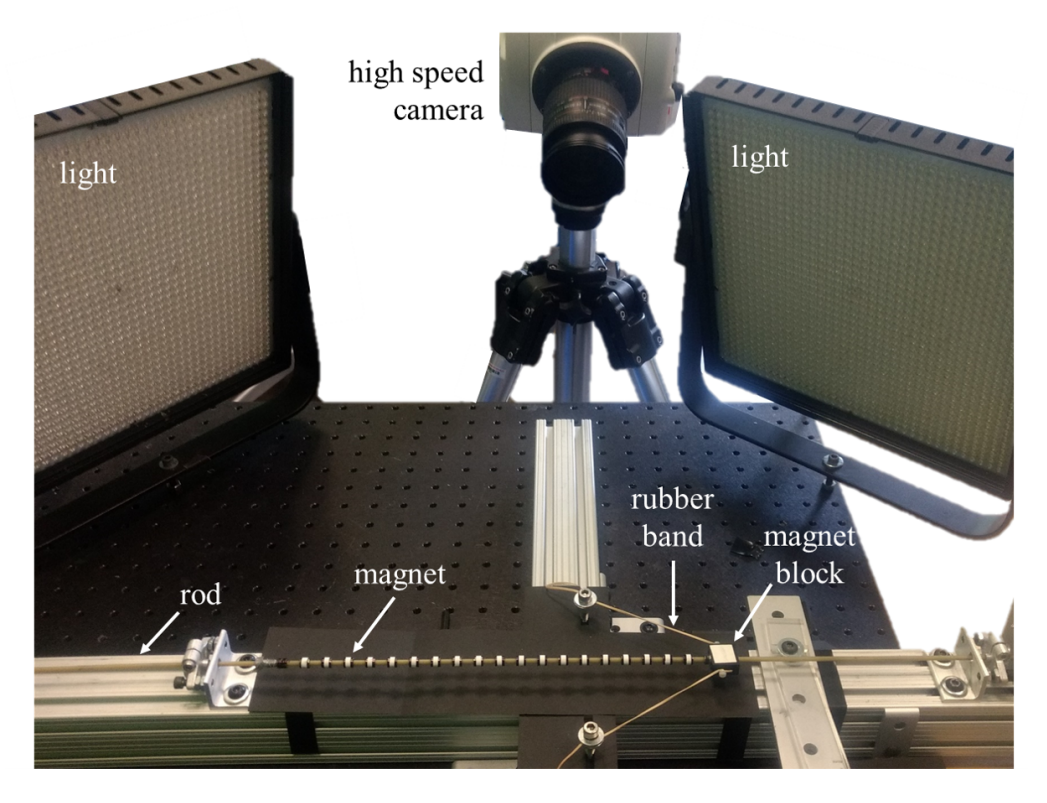


FIG. S1. Experimental setup.

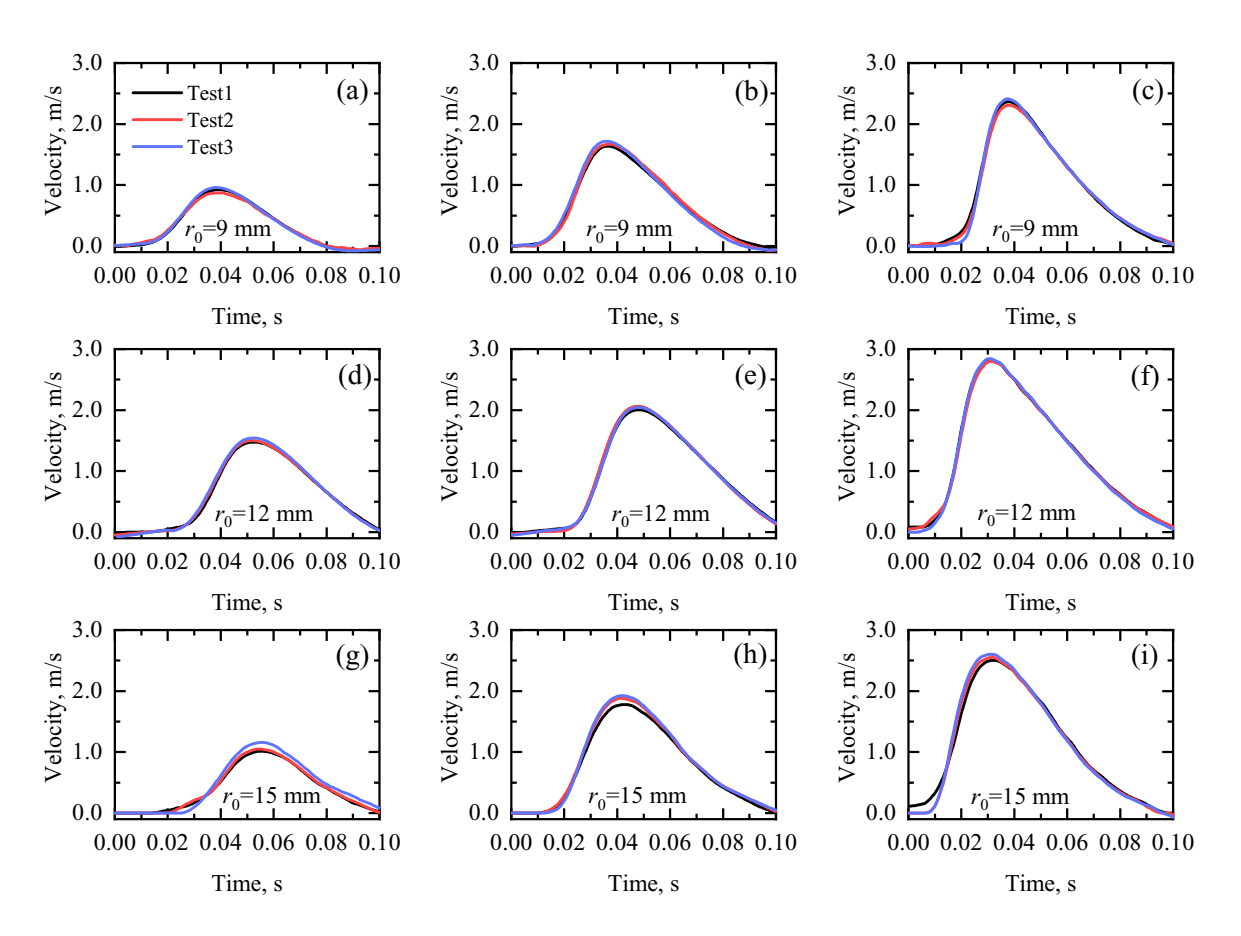


FIG. S2. Velocity profiles of the impact signal. Different rows show profiles obtained with different initial separations and thus represent systems with different initial stiffnesses. Different columns show profiles obtained for different impact strengths.

In experiments, different impact strengths are tuned by adjusting the pre-stretch of the rubber bands, and the stiffness of the system (by modifying the separation between magnets). Note that each set of experiment is repeated three times. The impactor velocity signals (i.e. the velocity profiles of the 1<sup>st</sup> magnet) are shown in Fig. S2.

#### S2. ESTIMATION OF UNCERTAINTY IN VELOCITY AND ACCELERATION DERIVATION

The finite resolution of images obtained via the high speed camera leads to an uncertainty in the measured magnet displacement. This uncertainty propagates to the derivation of the velocity and acceleration. Assuming images with space resolution  $\delta$  are recorded at sampling frequency f, we obtain a discrete time series for the displacements as  $(s_1, t_1), (s_2, t_2),...,(s_n, t_n)$  via DIC. The uncertainty in displacement is  $\Delta s = 0.5\delta$ . To calculate the velocity at time  $t_k$ , an interval of l measurements can be used to write

$$V = \frac{s_{k+l} - s_k}{t_{k+l} - t_k} = \frac{s_{k+l} - s_k}{l} f.$$
 (S1)

Since the uncertainty of sampling frequency f is very small [S1], we neglect its effect and the velocity uncertainty can be calculated as

$$\Delta V = \frac{\delta}{l} f. \tag{S2}$$

Accordingly, for the same chosen interval, l, the acceleration uncertainty can be calculated as

$$\Delta A = \frac{2\Delta V}{l} f = \frac{2\delta}{l^2} f^2. \tag{S3}$$

From Eqs. (S2) and (S3) it can be seen that for a given spatial resolution and sampling frequency, the larger the interval, l, the smaller the uncertainty in the estimation of the velocity and acceleration. On the other hand, the larger the interval that is used, the more loss of accuracy in estimation of the instantaneous velocity and acceleration. For our system, to compromise between uncertainty and accuracy, we select l=15. Given the space resolution  $\delta=0.30$  mm and sampling frequency 8 kHz, the uncertainties of velocity and acceleration are directly obtained from Eqs. (S2) and (S3), as  $\Delta V=0.16$  m/s, and  $\Delta A=170.67$  m/s<sup>2</sup>.

#### S3. MEASUREMENT OF THE MAGNETIC INTERACTION FORCE

To quantify the magnetic interaction force, we develop a setup to measure the 1<sup>st</sup> neighbor and 2<sup>nd</sup> neighbor interactions. As shown in Fig. S3, three magnets are aligned with opposite polarity (i.e. [N-S]-[S-N]-[N-S]) as in the chain magnet, thus the nearest interaction is a repulsive force, while the 2<sup>nd</sup> nearest interaction is an attractive force. The gap between the 2<sup>nd</sup> magnet and the 3<sup>rd</sup> magnet is fixed at a prescribed separation  $r_0$ . Using an Instron universal testing instrument we displace the 1<sup>st</sup> magnet along the vertical direction and measure the interaction force. We then employ the principle of superposition to recover the magnet force for the nearest interaction (i.e. with  $r_0 \to \infty$ ) and 2<sup>nd</sup> nearest interaction. Fig. S3 shows that the 2<sup>nd</sup> nearest interaction force is about 5% of the nearest interaction force, thus the non-nearest interaction is not considered in the numerical model.

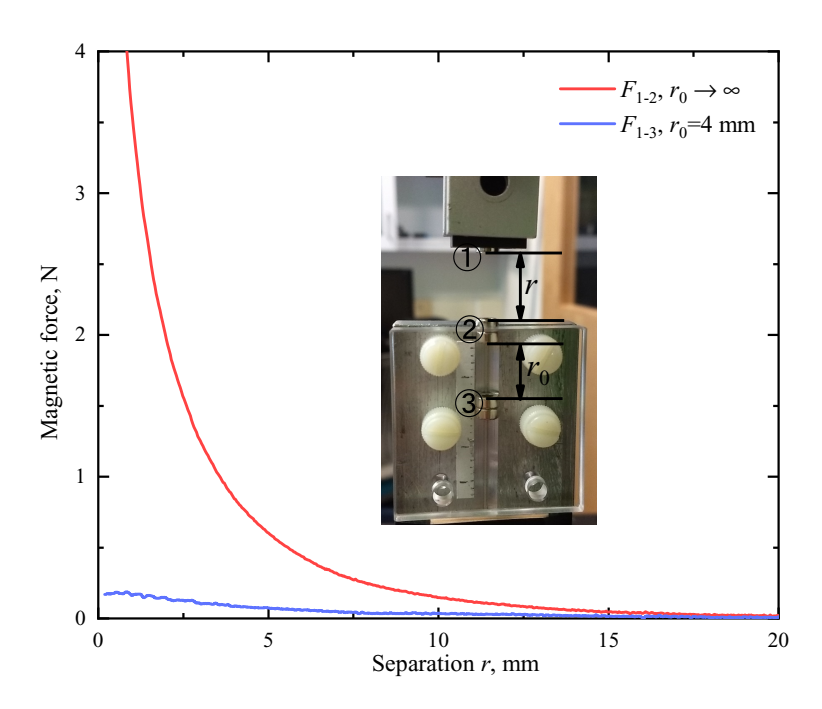


FIG. S3. Magnetic force for the nearest interaction  $F_{1-2}$  and the 2th nearest interaction  $F_{1-3}$ .

## S4. CALIBRATION OF THE COULOMB FRICTION COEFFICIENT

Here we quantify the value of friction in our experimental system. The Coulomb friction model, which assumes that the friction force is proportional to the normal contact force, is employed. Fig. S4(a) illustrates the magnetic forces acting on a particle within the lattice. Since the non-nearest interaction is much weaker than the nearest interaction (as shown in Fig. S3), only the nearest interaction force is considered. Hence, along the horizontal direction, the repelling forces are  $F_{1-2}$  and  $F_{3-2}$ . Additionally, the repelling/attracting force couples induce a torque which is denoted by  $M_{1-2}$  and  $M_{3-2}$ , respectively. Given the horizontal orientation of the lattice, gravitation induces a normal force mg, where m is the particle mass. Reactions from the suspending rod constrain the particle against rotation and translation in the vertical direction. The contact between the particle and the rod adds to the normal force, which contributes to the frictional force and thus resists to sliding of the magnets. We model the normal force as an additive contribution of the gravitational force and the reaction to the torque, which is proportional to the sum

of the repelling forces (i.e.  $F_{1-2} + F_{3-2}$ ) as

$$f_2 = \mu(mg + p(F_{1-2} + F_{3-2})),$$
 (S4)

where  $\mu$  is the Coulomb friction coefficient and p is an unknown dimensionless scaling coefficient. Both are determined via a dedicated calibration method, as detailed next. First, as shown in Fig. S4(b), we conduct an experiment in the system with three magnet particles. In particular, the left magnet and the right magnet are fixed at a certain separation  $r_1$ , the central magnet is displaced towards the left magnet with a separation  $r_0$ . Then, upon removing the applied force, the central magnet oscillates between two fixed magnets with a decaying amplitude (due to the existence of friction) until reaching a static equilibrium. In calibration experiments,  $r_0$  is set to be constant (i.e.  $r_0 = 1.8$  mm), while  $r_1$  varies from 249.5 mm to 30.1 mm. Finally, using the hypothesised friction law (i.e. Eq. (S4)) we solve the equation of motion for the one-degree-of freedom damped vibration of the central magnet, using the appropriate boundary conditions. The coefficients are then estimated by fitting to the experimentally measured results. Through this procedure, we obtain  $\mu = 0.285$  and p = 0.012. Figs. S4(c-h) shows the comparison between experimental and numerical results with the fitted coefficients. We observe an excellent agreement over a wide range of oscillation amplitudes. It is worth noting that, due to friction, the central magnet need not return to its central position as it reaches a new equilibrium state. When the initial separation between the left magnet and right magnet is small, the repulsive forces are dominant and the central magnet finds equilibrium at the central position (see Figs. S4(g,h)). However, when the initial separation is large, the friction force is dominant, and thus the final position of the central magnet significantly depends on the friction (see Figs. S4(a,b)).

#### S5. DYNAMIC RESPONSE OF A LINEAR LATTICE

For comparison with the nonlinear response provided in the main text, in Fig. S5 we provide results for a linear lattice under constant impact velocity. Here, the linear lattice implies that the interaction force between neighboring particles is proportional to the particle separation, namely F = kr, and k represents the stiffness. As shown in Fig. S5(a) for n = 20, upon arrival of the wave front, the particle velocity rapidly increases to a peak value, then oscillates with a decaying amplitude about the impactor velocity. Moreover, the propagation velocity gradually decreases and asymptotically approaches the analytical linear wave velocity (see Fig. S5(b)). In terms of first peak velocity and acceleration, Fig. S5(c) shows that the larger magnet number has a larger first peak velocity, but a smaller first peak acceleration, which is opposite to nonlinear stiffening system (the larger magnet number has a larger acceleration, see Fig. 3c). In Figs. S5(d) and (e), we find that both the oscillation amplitude and the period decrease with the increase of propagation time; in particular, the oscillation amplitude eventually decays completely.

#### S6. EFFECT OF FRICTION ON PROPAGATION VELOCITY

Fig. S6 reports the effect of friction on the propagation velocity in the nonlinear lattice. Our results reveal that the friction dramatically affects the propagation velocity. When no friction is considered, the propagation velocity eventually approaches a constant value. However, even vanishing levels of friction eventually lead to decay of the propagation velocity. In addition, systems with larger values of the friction coefficient exhibit a more dramatic decrease in the propagation velocity.

#### S7. EFFECT OF LOADING PROFILE IN THE NONLINEAR SYSTEM

Here we investigate the effect of the loading profile on the dynamic response of the nonlinear system. We first discuss the case characterized as a linear ramp - constant impact velocity (as shown in Fig. S7(a)). Fig. S7(b) shows that the loading profile with a longer acceleration time,  $T_r$  (i.e. smaller acceleration) requires a longer propagation time to reach the steady propagation velocity, while the steady propagation velocity is independent of the acceleration time. Moreover, Figs. S7(c,d) show that the stabilized oscillation amplitude and frequency are also independent of the acceleration time.

When considering a sinusoidal pulse impact wave (illustrated in Fig. S8a), the steady propagation velocity decreases dramatically when the signal duration time is smaller than the linear oscillation period,  $T_0$ , of the system (Fig. S8b). Moreover, when  $T_s << T_0$ , the steady propagation velocity tends to the linear propagation velocity; when  $T_s >> T_0$  the steady propagation velocity approaches the propagation velocity of the case with constant impact velocity. After passing through the pulse wave, Figs. S8(c,d) shows that the particle oscillates rapidly decrease in both amplitude and period, until the amplitude finally vanishes, implying that the particles eventually reach a static equilibrium state.

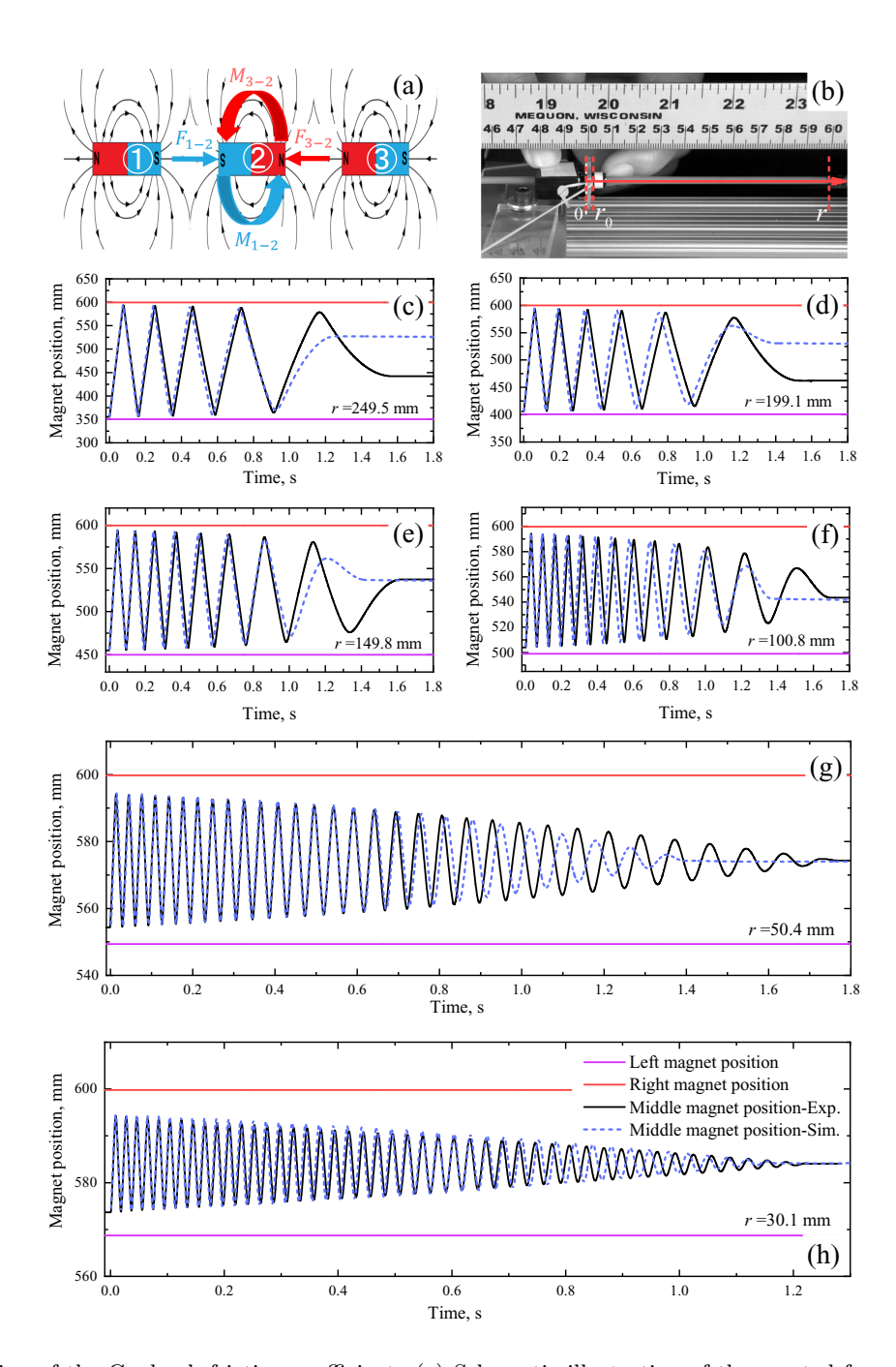


FIG. S4. Calibration of the Coulomb friction coefficient. (a) Schematic illustration of the exerted force and moment by the nearest magnet. (b) Calibration experiment setup. (c-h) Comparison of experimental (continuous back curves) and numerical (dashed blue curves) results on the central magnet position under different initial magnet separations. The numerical results are obtained with friction coefficients  $\mu=0.285$  and p=0.012.

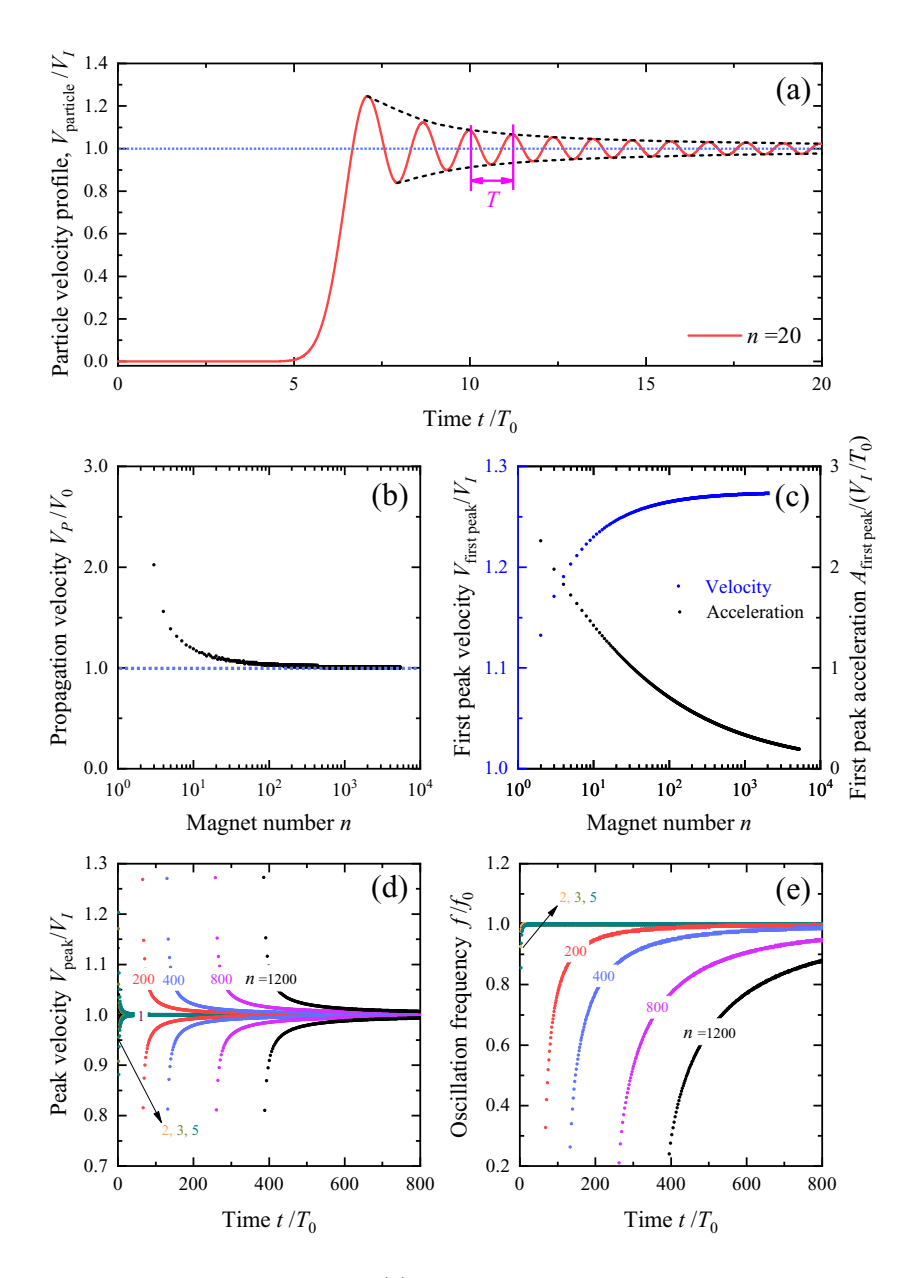


FIG. S5. Dynamic response of the linear lattice. (a) Typical velocity profile for a linear chain system under constant impact velocity. Dependence of propagation velocity (b), first peak velocity and first peak acceleration (c) on particle number. Evolution of peak velocity (d) and oscillation frequency (e) with time for various particles. Note that for the linear chain system with stiffness k and particle separation  $r_0$ , the linear propagation velocity is  $V_0 = r_0 \sqrt{k/m}$ , the oscillation frequency is  $f_0 = 1/\pi \sqrt{k/m}$ , and the oscillation period is  $T_0 = 1/f_0$ .

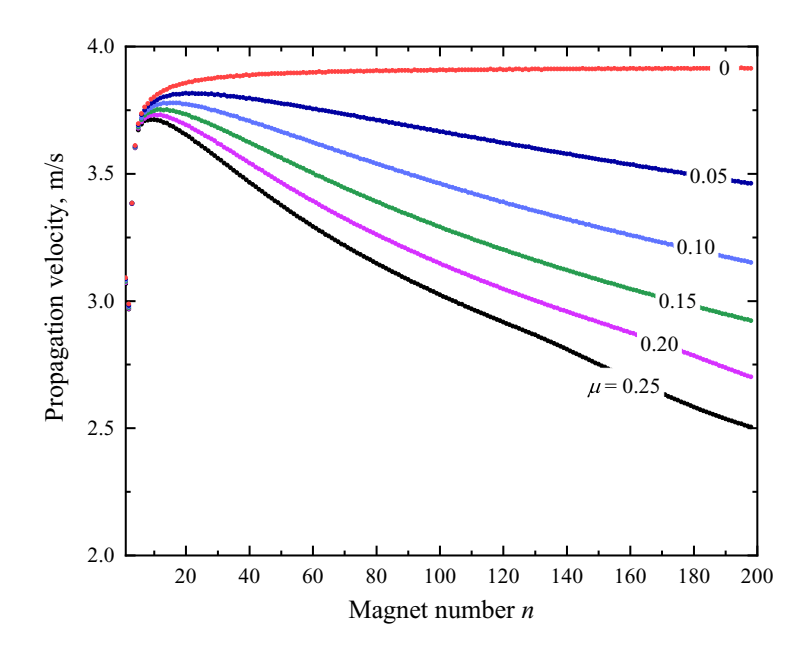


FIG. S6. Effect of friction on propagation velocity. Results are obtained by the calibrated simulation model with the approximated friction force law (i.e. Eq.(S4)) and initial magnet separation  $r_0 = 12$  mm under constant impact velocity  $V_I = 2$  m/s.

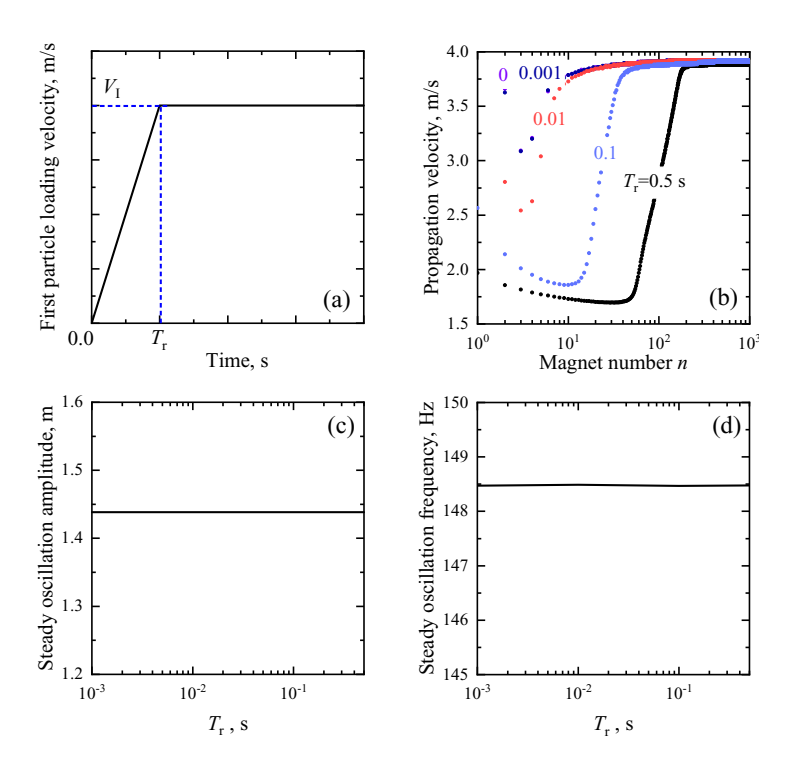


FIG. S7. (a) Schematic illustration of the ramp-constant velocity loading profile. (b) Dependence of propagation velocity on magnet number. Steady oscillation amplitude (c) and oscillation frequency (d) verse ramp time  $T_{\rm r}$ . Results are obtained by the calibrated simulation model with initial magnet separation  $r_0=12$  mm and neglecting friction.

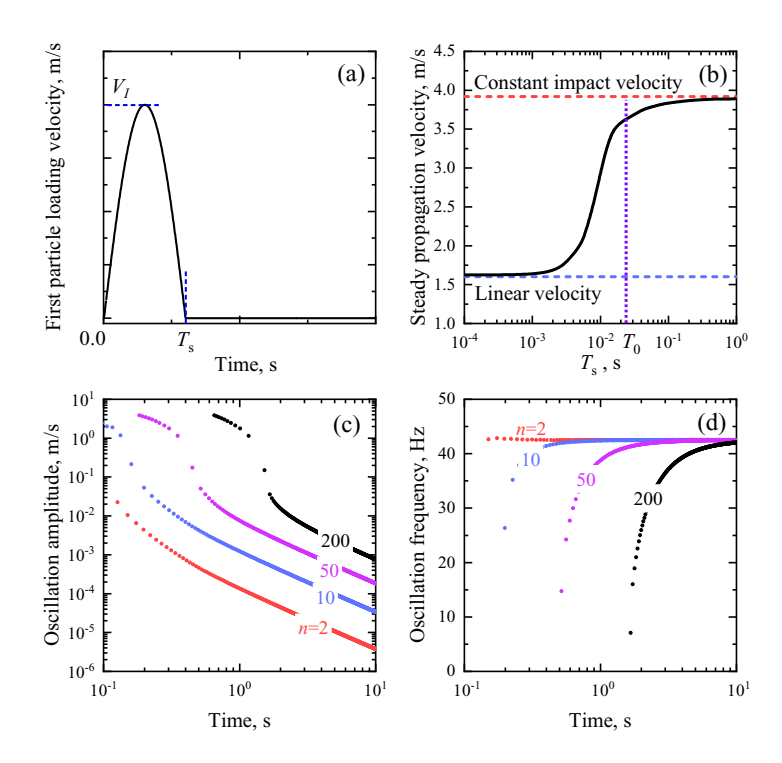


FIG. S8. (a) Schematic illustration of the velocity profile for a sinusoidal pulse impact wave. (b) Dependence of stabilized propagation velocity on signal duration time  $T_s$ , the peak impact velocity is set to be  $V_I=2$  m/s. Oscillation amplitude (c) and oscillation frequency (d) verse propagation time, the signal duration time  $T_s=0.1$  s and  $V_I=2$  m/s are considered. Results are obtained by the calibrated simulation model with initial magnet separation  $r_0=12$  mm and neglecting friction.

#### S8. QUANTITATIVE COMPARISON OF MAGNETIC SYSTEM AND COPPER ATOM LATTICE

To establish a quantitative comparison of the proposed magnetic lattice system with the response of atomic scale lattices, we examine the properties of the magnetic lattice with separation  $r_0=12$  mm in comparison to a copper atom lattice with a classical Lennard-Jones potential [S2]

$$\phi(r) = 4\epsilon \left[ \left( \frac{\sigma}{r} \right)^{12} - \left( \frac{\sigma}{r} \right)^{6} \right], \tag{S5}$$

where r denotes the separation between atoms,  $\epsilon = 6.55 \text{e-}20 \text{ J}$  is the depth of the potential well,  $\sigma = 2.34 \text{e-}10 \text{ m}$  is the distance at which the atom-atom potential energy is zero. Table S1 summarizes physical properties of the copper atom lattice alongside those of the magnetic lattice. It is shown that through scaling particle mass, and lattice separation, while preserving a similar stiffness, the linear propagation velocity is scaled down by three orders of magnitude. This reduction in propagation speed is key for our observations via high-speed camera. Interestingly, despite scaling the size of the system by 8 orders of magnitude, our proposed macroscopic magnet lattice system preserves the key quantitative features of shock wave propagation as the atomic system: both our magnetic system and the copper atomic model show that shock propagation velocity is nearly linearly dependent on the impactor velocity with a coefficient  $\sim 1$  (Figs. S9(a,c)). Additionally, the critical velocity (for onset of strong shock waves) is of the same order of magnitude as the linear propagation velocity (Figs. S9(b,d)). These similarities further support our approach of experimentally studying shock wave behavior at the molecular scale via a macroscopic desktop-scale system.

TABLE S1. Comparison of physical properties of magnetic system and copper atom lattice. The linear stiffness of the copper lattice is calculated at the equilibrium separation  $r = r_0$  as  $d^2 \phi / dr^2$ .

	Particle mass [kg]	Lattice separation [m]	Stiffness [N/m]	Linear propagation velocity [m/s]
Copper atom lattice	1.055e-25	2.63e-10	68.36	6.69e3
Magnetic lattice	1.084e-3	1.20e-2	19.31	1.60

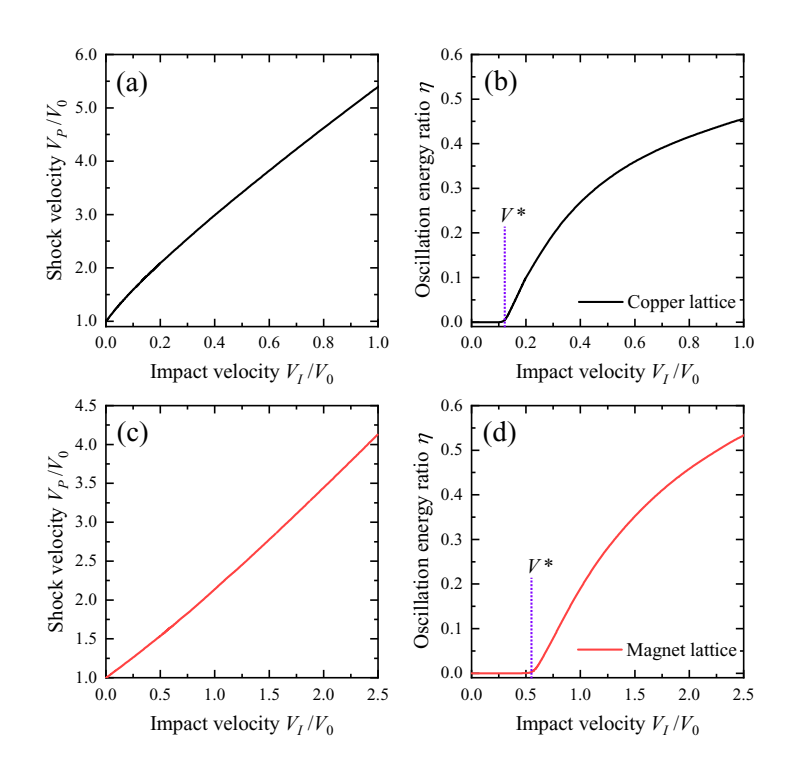


FIG. S9. Dynamic response of shock wave in copper atom lattice with Lennard-Jones potential (a, b) and in magnetic system with  $r_0$ =12 mm (c, d). Results are given for the shock propagation velocity (a, c) and oscillation energy ratio (b, d).

# S9. EFFECT OF IMPACTOR VELOCITY ON THE DYNAMIC RESPONSE OF THE NONLINEAR SYSTEM

Here we show the effect of the impactor velocity on the dynamic response of the nonlinear system. Fig. S10 shows the particle velocity as a function of magnet separation. Upon the arrival of the shock front, the particle velocity rapidly increases and oscillates about the impactor velocity. Remarkably, when moderate impactor velocity is considered, the particle finally reaches a steady state in which it adopts the velocity of the impactor (see Figs. S10(a) and (b)); however, as the impactor velocity exceeds a threshold value, the particle at long propagation time exhibits a steady oscillation about the impactor velocity, altering the particle kinetic energy and system potential energy (see Figs. S10(c) and (d)). Moreover, it is observed that the larger impactor velocity takes less transition cycles to reach the steady oscillatory state.

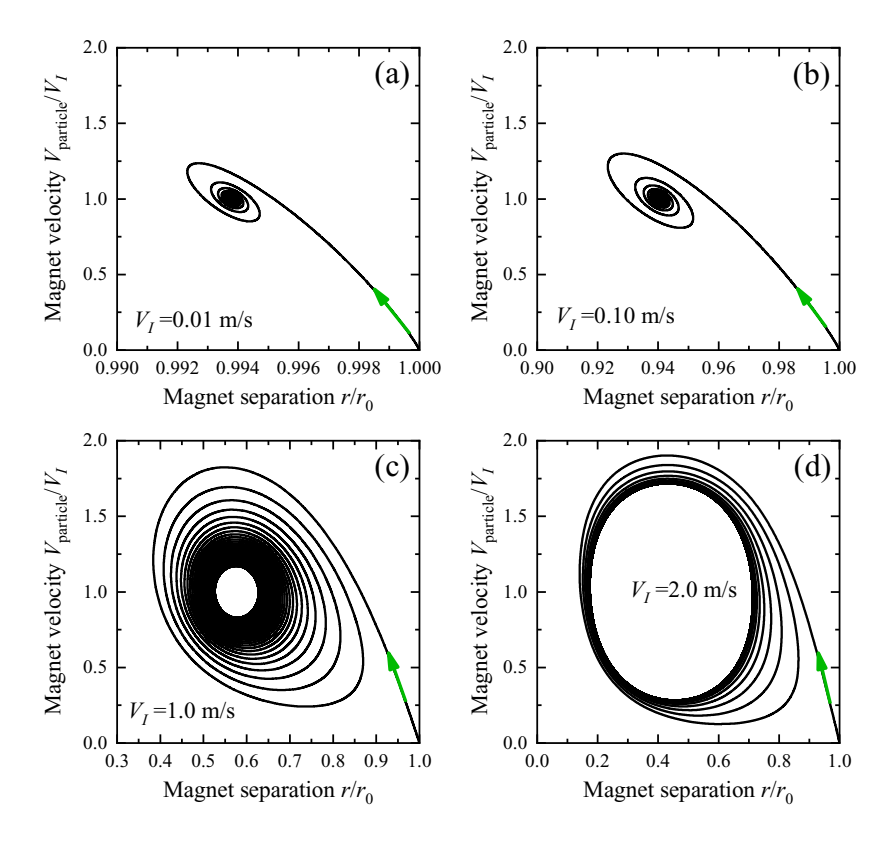


FIG. S10. Particle velocity versus magnet separation for various impactor velocities. (a)  $V_I = 0.01$  m/s, (b)  $V_I = 0.10$  m/s, (c)  $V_I = 1.0$  m/s, (d)  $V_I = 2.0$  m/s. Results are given for the  $10^{\text{th}}$  magnet and are obtained by the calibrated simulation model with initial magnet separation  $r_0 = 12$  mm and neglecting friction under constant impact velocity. The magnet separation is calculated as the gap between the  $10^{\text{th}}$  and  $11^{\text{th}}$  magnets.

<sup>[</sup>S1] C. Robbe, N. Nsiampa, A. Oukara, and A. Papy, Quantification of the uncertainties of high-speed camera measurements, International Journal of Metrology and Quality Engineering 5, 201 (2014)

<sup>[</sup>S2] Ş. Erkoç, Empirical potential energy functions used in the simulations of materials properties, Annual Reviews Of Computational PhysicsIX, 1 (2001)